Estimation of Cirrus Optical Thickness from Sun Photometer Measurements

MASATAKA SHIOBARA AND SHOJI ASANO

Meteorological Research Institute, Tsukuba, Japan

(Manuscript received 26 July 1993, in final form 1 December 1993)

ABSTRACT

A method is proposed to estimate the optical thickness of cirrus clouds from ground-based sun photometry. Transfer calculations of solar radiation in ice clouds were made by the Monte Carlo method. A scattering phase function presented by Takano and Liou was employed for ice clouds. Simulations of sun photometry, which include strong forward scattering into the instrument's field of view, give a simple relationship between the true and apparent optical thicknesses. The correction method was applied to sun photometer measurements for cirrostratus clouds observed at Tsukuba, Japan. The relationship between the visible optical thickness and the broadband solar flux transmittance obtained from observations agreed well with that theoretically expected for cloud optical thickness up to about 10.

1. Introduction

Cirrus and cirrostratus clouds, which consist of ice crystals and are located in the upper troposphere and are optically thin, play an important role in the earth radiation budget and hence in the earth's climate system. However, we have insufficient knowledge of their radiative and microphysical properties. Several field experiments to improve our knowledge of such clouds have been conducted successively in the last decade [International Cirrus Experiment (ICE 1989); First ISCCP (International Satellite Cloud Climatology Project) Regional Experiment (FIRE 1990); Western North Pacific Cloud Radiation Experiment (WENPEX/MRI 1992)].

The optical thickness is one of the essential parameters for expressing radiative properties of clouds. In order to obtain the optical thickness of cirrus, we have measured the direct solar transmission using a sun photometer. Under cirrus clouds, however, a sun photometer with a finite field of view (FOV) measures not only the attenuated direct radiance but also the scattered radiance, since ice crystals in such clouds yield extremely strong forward scattering. Thus the radiance scattered into the sun photometer's FOV may result in erroneous transmission, and hence the optical thickness may be underestimated. Raschke and Cox (1983) presented a method to deduce the cloud optical thickness from multi-FOV photometer measurements. Their estimation was for water clouds, however.

In this study, we have carried out an extensive radiative transfer calculation to simulate sun photometer measurements of ice clouds by taking into account the strong forward scattering by ice crystals into the instrument's FOV. A Monte Carlo method was applied in the simulation. We employed the scattering phase function for ice crystals calculated by Takano and Liou (1989, hereafter referred to as TL).

Using the Monte Carlo simulations, we have derived a simple relationship between the true and apparent optical thicknesses. The result shows that the apparent solar transmittance including radiance scattered into the FOV can be parameterized with the slant-path optical thickness if the scattering phase function for ice clouds is known. The correction method is applied to sun photometer measurements of cirrostratus clouds observed at Tsukuba, Japan. The relationship between the cirrus optical thickness and the solar flux transmittance is discussed.

2. Instrument and measurements

Spectral solar transmission measurements were acquired by a model MS-115 sun photometer manufactured by Eko Instruments Co., Tokyo, Japan. The sun photometer uses a silicon photodiode to detect light in the visible to near-infrared region. The instrument's FOV is circular, and the half-FOV angle $\eta_0 = 1.2°$ is determined by geometry between an aperture facing the sun and a field-limit pinhole in front of the detector. There are eight interference filters with peak transmissions at the wavelengths λ = 368, 421, 502, 676, 760, 864, 938, and 1050 nm, and full widths of the half maximum transmission $\Delta\lambda$ = 4–6 nm. In general, aerosol observations utilize all wavelengths except for 760 and 938 nm, which are, respectively, selected at oxygen and water vapor absorption bands. The instrument employs a filter wheel rotating at the rate of 120

Corresponding author address: Dr. Masataka Shiobara, Climate Research Department, Meteorological Research Institute, 1-1 Nagamine, Tsukuba 305, Japan.

rpm on which the eight filters are installed. The sample-and-hold circuits and independent amplifiers for the eight channels allow data to be acquired simultaneously for all channels. The internal temperature for the electronics and optics is controlled at a constant 40°C. The sun tracking is accomplished by an equatorial drive with a synchronous motor. In our system, dc voltage signals from the eight channels are digitized by a data logger with analog-to-digital (A/D) converters at an arbitrary interval longer than 1 s and are then stored in a magnetic device through a personal computer.

The observations reported here were conducted at the Meteorological Research Institute (MRI, 36.05°N, 140.13°E, 31 m MSL), Tsukuba, Japan, on 22 and 30 June 1989 as part of the MRI program of the WENPEX in the Japanese World Climate Research Programme activities (WENPEX/MRI 1992). Simultaneous measurements were carried out with the Hydrometeor Video Sonde System (HYVIS) developed at MRI (Murakami and Matsuo 1990) and a lidar system (Uchino et al. 1988), as well as ground-based radiation measurements (Uchiyama et al. 1993).

3. Monte Carlo simulations

Monte Carlo methods have been used for radiative transfer calculations, especially for cases that contain anisotropic scattering media or non-plane-parallel atmosphere. The Monte Carlo method has another advantage; it is easy to include scattering phase functions with extremely large forward peaks and to evaluate each order of scattering. In this study, radiative transfer of solar radiation in a homogeneous plane-parallel atmosphere is simulated by a forward Monte Carlo method. Polarization is not considered. The geometry for scattering is illustrated in Fig. 1. Transmission of radiation along a path s is given by

$$T = \exp\left(-\int_0^s \beta ds\right) = \exp(-\bar{\tau}), \tag{1}$$

where β is the volume extinction coefficient along the path, and $\bar{\tau}$ is the slant-path optical length given by the integral of β over the path. When a horizontally homogeneous atmosphere is assumed, the location of a scattered photon τ_i, that is, the vertical optical thickness above the position of the photon to the top of the atmosphere, is given by

$$\tau_i = \tau_{i-1} + \bar{\tau}\cos\theta, \tag{2}$$

where θ is the zenith angle of the photon's path. When a new photon enters the top of the atmosphere, θ of the photon is equal to θ_0, that is, the solar zenith angle. Transmission is equivalent to the probability of a photon reaching $\bar{\tau}$, and the slant-path length $\bar{\tau}$ of a traveling photon is determined by the following equation, with the probability p_t given as a random number that takes a value between 0 and 1:

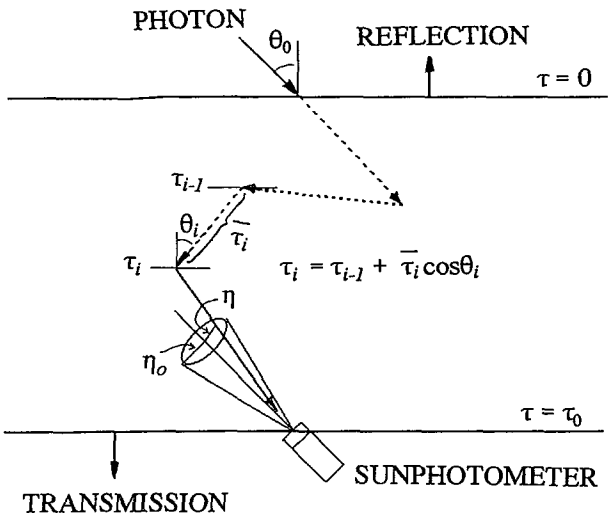

FIG. 1. Geometry for scattering of a photon.

$$\bar{\tau} = -\ln(p_t). \tag{3}$$

Figure 2 shows a schematic flow of the Monte Carlo simulation. A new photon travels from $\tau = 0$, that is, the top of the atmosphere, to $\tau = \tau_1$. The photon then collides with a scattering medium if $\tau_1 < \tau_0$, where τ_0 is the vertical optical thickness at the bottom of the atmosphere. The scattering angle Θ, that is, the direction of the photon after collisions, and the azimuthal angle Φ, that is, the angle around the scattering axis, are determined by

$$p_\Theta = \int_0^\Theta P(\Theta)\sin\Theta d\Theta, \tag{4}$$

$$\Phi = 2\pi p_\Phi, \tag{5}$$

where p_Θ and p_Φ are the probabilities, which are also given by random numbers taking values between 0 and 1, with respect to the scattering direction (Θ, Φ). The energy of a photon, E_i, is reduced by the single scattering albedo $\bar{\omega}$ for each collision as

$$E_i = \bar{\omega} E_{i-1} \quad (E_0 = 1). \tag{6}$$

The normalized phase function $P(\Theta)$ and the single scattering albedo $\bar{\omega}$ are defined as follows:

$$\int_0^\pi P(\Theta)\sin\Theta d\Theta = 1, \tag{7}$$

$$\beta\bar{\omega}P(\Theta) = \beta_c\bar{\omega}_c P_c(\Theta) + \beta_a\bar{\omega}_a P_a(\Theta) + \beta_R\bar{\omega}_R P_R(\Theta), \tag{8}$$

$$\bar{\omega} = \beta^{-1}(\beta_c\bar{\omega}_c + \beta_a\bar{\omega}_a + \beta_R\bar{\omega}_R), \tag{9}$$

$$\beta = \beta_c + \beta_a + \beta_R, \tag{10}$$

where the subscripts c, a, and R correspond to clouds, aerosols, and Rayleigh scattering, respectively. Random numbers are generated by the linear congruential

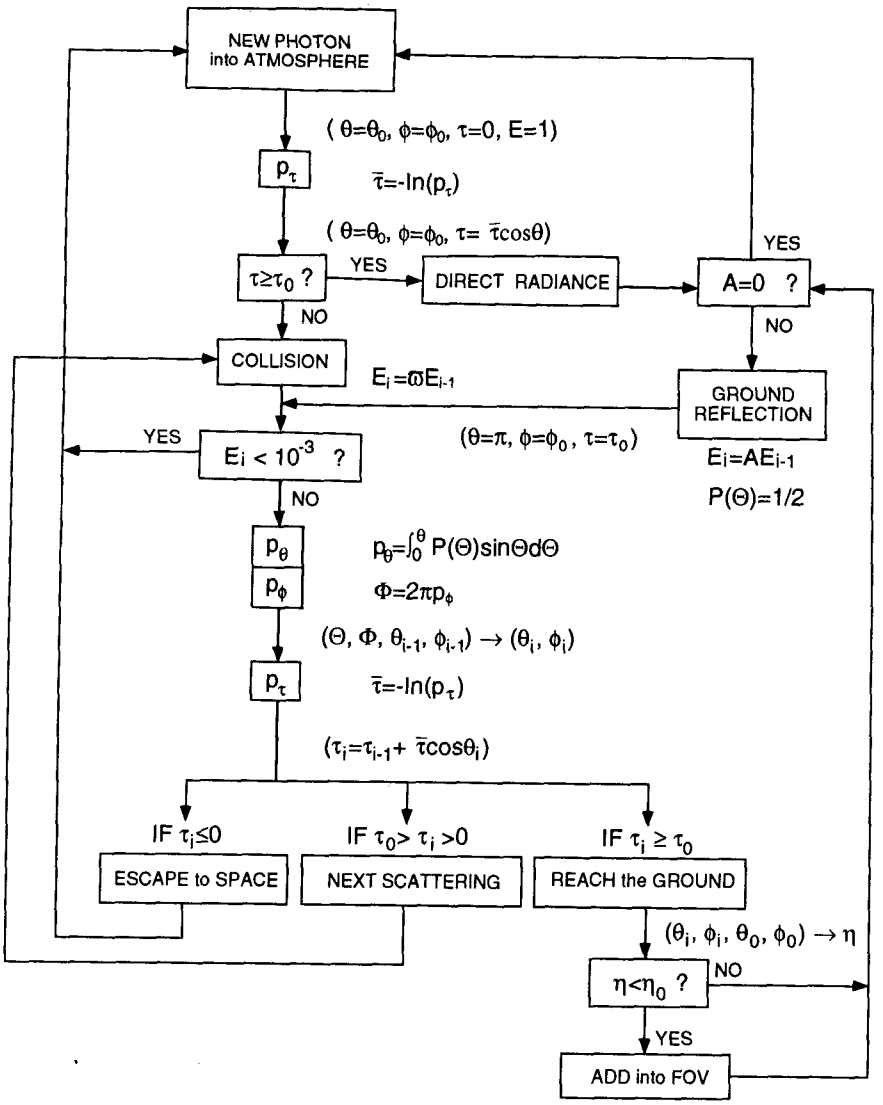

FIG. 2. A schematic flow of the Monte Carlo simulation.

method using a subprogram supplied by NEC for personal computer users (NEC 1991, personal communication). The direction of a photon after a collision, (θ_i, ϕ_i), is given by the direction prior to the collision $(\theta_{i-1}, \phi_{i-1})$ and the scattering angles (Θ, Φ) using the following relations derived from spherical trigonometry:

$$\cos\theta_i = \cos\theta_{i-1}\cos\Theta + \sin\theta_{i-1}\sin\Theta\cos\Phi, \quad (11)$$

$$\cos\Theta = \cos\theta_i\cos\theta_{i-1} + \sin\theta_i\sin\theta_{i-1}\cos(\phi_i - \phi_{i-1}). \quad (12)$$

The photon's travel terminates when the subsequent collision takes place outside the boundaries, that is, at $\tau_i < 0$ or $\tau_i > \tau_0$, or when the energy of the photon becomes $E_i < 10^{-3}$. When a photon reaches the ground, and if the angle between the solar axis and the scattering axis, η given as

$$\cos\eta = \cos\theta_i\cos\theta_0 + \sin\theta_i\sin\theta_0\cos(\phi_i - \phi_0), \quad (13)$$

is smaller than the half-FOV angle η_0, the photon is detected by the instrument. If the ground surface albedo $A \neq 0$ is taken into account, the photon that reaches the ground is reflected to the atmosphere with the probability of A. The isotropic reflection at the ground surface is included in our Monte Carlo scheme. In practice, however, the surface albedo is assumed to be zero unless otherwise stated in this study.

Our study employs the scattering phase function for ice crystals given in Table 1 of TL. The phase function was calculated at $\lambda = 0.55$ μm for a cirrostratus model based on the observational results presented by

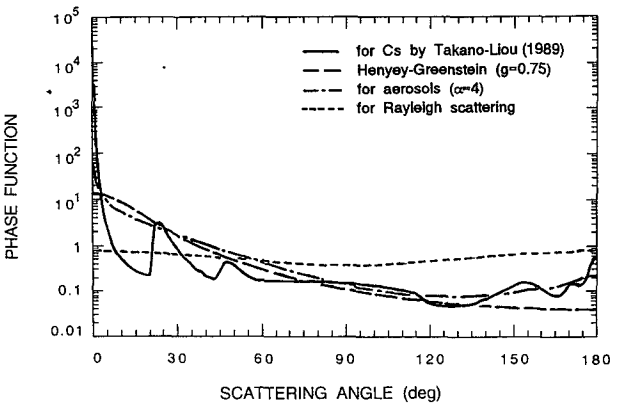

FIG. 3. Phase functions for Rayleigh scattering (short-dashed line), and scattering by aerosols (dotted–broken line), and ice crystals (solid line). A Henyey–Greenstein phase function with $g = 0.75$ is shown by the broken line.

Heymsfield (1975). The phase functions for Rayleigh scattering and scattering by aerosols and ice crystals are compared in Fig. 3. The corresponding sky radiance is shown in Fig. 4a for Rayleigh scattering, Fig. 4b for aerosol scattering, and Fig. 4c for ice clouds, respectively. The phase function for aerosols was calculated for spherical particles with a power-law size distribution as described later. Since Fig. 4 employs a zenithal equidistance projection, the center of each panel is the zenith and the circular outline is the horizon. Each dot in the figure indicates the direction (θ, ϕ) of a photon reaching the ground. In Fig. 4c, the 22° halo is clearly found while the 46° halo is vague. It should be noticed that the density of dots in the figure does not directly reflect the intensity of scattered radiation. In this study, only the direction of photons is taken into account and the density of photons expresses the contribution of radiance to the global flux. As a result, the sky around the horizon seems rather dark in the figure.

The accuracy of our Monte Carlo code was investigated by comparing with exact values of the direct transmission T, given by Eq. (1), and also by comparing with values of the diffuse flux transmittance $F^{\downarrow}$ and the flux reflectance $F^{\uparrow}$ from the doubling-method calculation in Tables 35 and 37 of van de Hulst (1980). The Henyey–Greenstein phase function (hereafter referred to as HG) was used in the comparison. Table 1 contains the results for several cases with the asymmetry factor $g = 0.25$, 0.5, and 0.75, and the single scattering albedo $\bar{\omega} = 0.6$, 0.8, and 1.0. The Monte Carlo results agree well with the values expected by Eq. (1) or by the doubling results DBL within a 0.005 difference.

Convergence conditions were also investigated with respect to the number of photons. Figure 5 shows an example indicating convergence with increase of photons. The simulations mostly converged within 10 000 photons. For simulations with 40 000 photons, T and $F^{\downarrow}$ converged at values with $\sigma = 0.0023$ and 0.0024, respectively. Differences between the doubling method result and the mean value of simulations for T and $F^{\downarrow}$ are 0.0014 and 0.0003, respectively. Thus, the Monte Carlo calculation in this study may have a 0.005 error at most. Forty thousand photons were used in the following simulations although results did not improve significantly beyond those with 10 000 photons.

4. Results and discussion

a. Estimation of cloud optical thickness

Figure 6 shows the solar transmissions obtained from simulations at the solar zenith angles $\theta_0 = 0°$, 30°, 60°, and 75° as a function of the slant-path optical thickness $\bar{\tau}_0$, which is defined as the column optical thickness τ_0 multiplied by the optical air mass m ($= \sec\theta_0$). A phase function from TL was used for ice clouds. The calculation was done for $\bar{\tau}_0 = 0.5$, 1, 2, 4, 6, 8, and 10 (Table 2). It is found from the figure that the apparent transmittance, that is, the direct solar transmission plus transmission due to scattering into the FOV, can be parameterized with the slant-path optical thickness as follows:

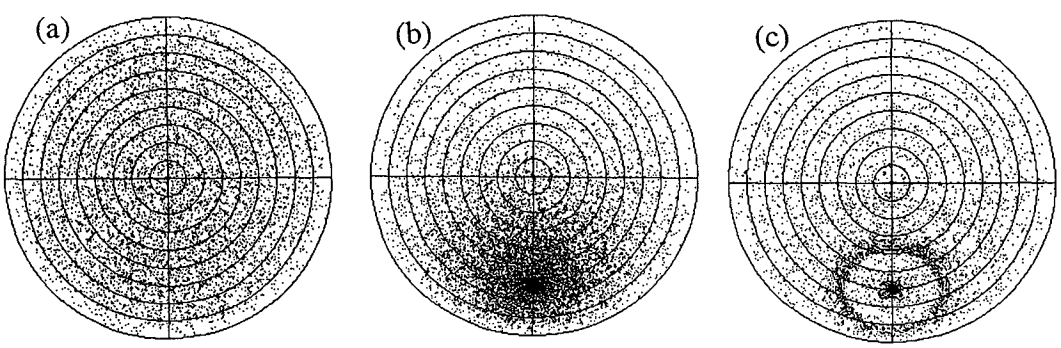

FIG. 4. Monte Carlo simulations of the sky radiance transmitted to the ground for (a) Rayleigh, (b) aerosol, and (c) ice-crystal atmospheres. A zenithal equidistance projection is employed. The optical thickness $\tau_0 = 0.5$ and the solar zenith angle $\theta_0 = 60°$ for all cases.

TABLE 1. Comparisons between the results from the present Monte Carlo method and the doubling method: T, $F^{\downarrow}$, and $F^{\uparrow}$ are the direct solar transmittance, the diffuse flux transmittance, and the flux reflectance, respectively. Further MC, Eq. (1), and DBL correspond to the Monte Carlo method, Eq. (1) in the text, and the doubling method, respectively.

				T		$F^{\downarrow}$		$F^{\uparrow}$	
g	$\bar{\omega}$	τ_0	θ_0	MC	Eq. (1)	MC	DBL	MC	DBL
0.25	1.0	0.5	0	0.6054	0.6065	0.2486	0.2464	0.1461	0.1471
		2	0	0.1327	0.1353	0.4329	0.4301	0.4345	0.4346
		1	60	0.1353	0.1353	0.4306	0.4247	0.4341	0.4400
0.5	1.0	0.5	0	0.6082	0.6065	0.3030	0.3037	0.0888	0.0898
		2	0	0.1328	0.1353	0.5437	0.5444	0.3236	0.3203
		1	60	0.1361	0.1353	0.5075	0.5029	0.3565	0.3618
0.75	1.0	0.5	0	0.6099	0.6065	0.3520	0.3562	0.0381	0.0373
		1	0	0.3707	0.3679	0.5503	0.5534	0.0789	0.0787
		0.5	60	0.3698	0.3679	0.4956	0.4954	0.1345	0.1367
		2	0	0.1350	0.1353	0.6996	0.7015	0.1653	0.1632
		1	60	0.1343	0.1353	0.6295	0.6242	0.2361	0.2405
		4	0	0.0170	0.0183	0.6692	0.6701	0.3136	0.3116
		2	60	0.0190	0.0183	0.6060	0.6067	0.3749	0.3750
0.75	0.8	1	0	0.3705	0.3679	0.3798	0.3804	0.0396	0.0403
		1	60	0.1357	0.1353	0.3834	0.3808	0.1191	0.1234
0.75	0.6	1	0	0.3704	0.3679	0.2503	0.2506	0.0208	0.0212
		1	60	0.1360	0.1353	0.2286	0.2276	0.0624	0.0649

$$T' = e^{-k\bar{\tau}_0}. \tag{14}$$

In this case, the least-squares fit to the result gives the correction coefficient $k = 0.521$. Another apparent transmittance, which was calculated for water clouds by Raschke and Cox (1983) using a Monte Carlo method, is also shown by the long-dashed curve in Fig. 6. The difference in the results might be caused by the different scattering phase functions for water droplets and ice crystals. The radiance singly scattered into the sun photometer's FOV, $P\Delta\Omega$, is defined by

$$P\Delta\Omega = \int_0^{\eta_0} P(\Theta) \sin\Theta d\Theta. \tag{15}$$

Using the TL phase function, $P\Delta\Omega$ for the FOV of $\eta_0 = 1.2°$ amounts to 49% of the radiance scattered in all directions. Therefore, even the single scattering transmission T_s in Table 2 is larger than the estimation by Raschke and Cox (1983). Here, T_s is estimated from the following equation assuming that η_0 is small:

$$T_s = \bar{\tau}_0 \bar{\omega} P\Delta\Omega e^{-\bar{\tau}_0}, \tag{16}$$

where $\bar{\omega} = 0.99999$ according to the TL calculation at $\lambda = 0.55$ μm for a cirrostratus model.

Further, the simulations show that the number of photons scattered more than twice exceeds that of photons scattered singly when the slant-path optical thickness is larger than 3.

We have also investigated how much the aerosol scattering affects the apparent transmission. Figure 7 shows the results for the aerosol scattering. The aerosol scattering phase functions were calculated by Mie scattering theory for two power-law size distributions with different powers, $\alpha = 3.5$ and 4.0, between particle radii of 0.1 and 15 μm. The two aerosol models with the same refractive index, $m^* = 1.55 - 0.01i$, have the single scattering albedo $\bar{\omega} = 0.87$ and 0.91, and the asymmetry factor $g = 0.70$ and 0.66, respectively. In the figure, the ordinate ΔT is defined as

$$\Delta T = \frac{T' - T}{T}. \tag{17}$$

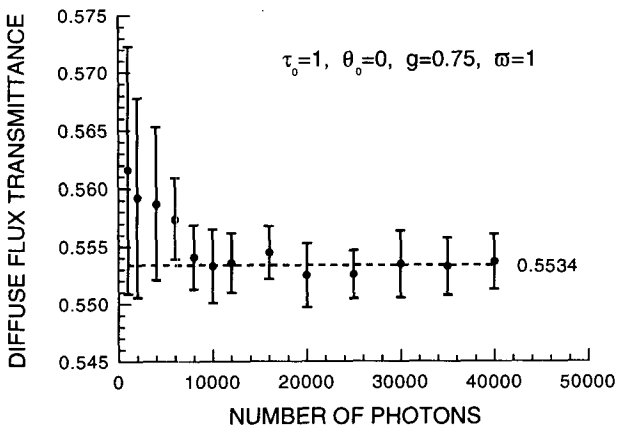

FIG. 5. Convergence of the Monte Carlo simulation for the case of the diffuse flux transmittance calculation where $\tau_0 = 1$, $\theta_0 = 0$, $g = 0.75$, and $\bar{\omega} = 1$. Five results using different seeds for the initial generation of random numbers were traced. Those results were averaged at the point where the same number of photons were generated and are indicated by solid circles with vertical bars representing the standard deviation. The value of 0.5534 is obtained from van de Hulst (1980).

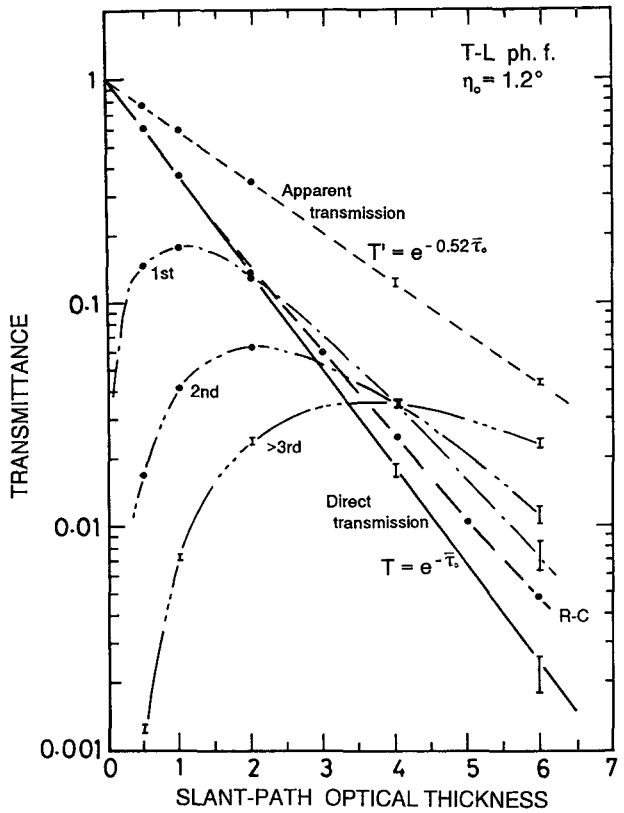

FIG. 6. Simulation results of solar transmission for various slant-path optical thicknesses of ice clouds when a sun photometer has a half-FOV $\eta_0 = 1.2°$. The TL phase function has been used. The thick solid curve indicates the true transmittance. Transmission into the instrument's FOV due to single scattering (1st), secondary scattering (2nd), and scattering over third orders (>3rd) are indicated by the dot–dashed, double dot–dashed, and triple dot–dashed curves, respectively. The short-dashed curve indicates the apparent transmittance. Error bars and solid circles attached to the curves indicate differences among the Monte Carlo results calculated for four different solar zenith angles with the same slant-path optical thicknesses. The long-dashed curve shows the apparent transmittance presented by Raschke and Cox (1983) in which water clouds are assumed.

Using ΔT along with Eq. (1), the following approximation is possible:

$$\bar{\tau}'_0 = \bar{\tau}_0 - \ln(1 + \Delta T). \tag{18}$$

The single scattering approximation expressed by Eq. (16) gives the following equation:

$$\Delta T = \bar{\tau}_0 \bar{\omega} P \Delta\Omega, \tag{19}$$

where $\bar{\omega} P\Delta\Omega = 0.009$ and 0.031 for the cases of $\alpha = 4$ and 3.5, respectively. The results in Fig. 7 indicate that the single scattering contribution is dominant in the transmission due to scattering into the FOV. Further, although the forward scattering into the FOV depends on the size distribution of aerosols, the effect on sun photometry is negligibly small for ordinary aerosol measurements since the scattering phase function for aerosols has a forward scattering peak much smaller than that for ice crystals.

Our results indicate that the apparent optical thickness τ'_0 can be simply related to the true optical thickness τ_0 for both cases of clouds and aerosols as follows:

$$\bar{\tau}'_0 = k\bar{\tau}_0, \tag{20}$$

with

$$k = 1 - \bar{\omega} P\Delta\Omega. \tag{21}$$

When the single scattering approximation is good for such cases as aerosols with small optical thicknesses, Eqs. (20) and (21) are consistent with Eqs. (18) and (19).

Table 3 shows the results for several cases of nonconservative scattering, that is, the single scattering albedo $\bar{\omega} \neq 1$. It is found from the table that Eq. (21) is valid also for these cases, as well as for the cases in Table 2, within a 0.005 difference. Figure 8 shows re-

TABLE 2. Simulations of sun photometer measurements for ice clouds. The Monte Carlo results for the direct solar transmittance T, the single scattering transmission T_s, and the apparent transmittance T' are compared with those in column EX, which were calculated by Eq. (1), Eq. (16), and Eqs. (14) and (21), respectively.

θ_0	0	30	60	75	
m	1	1.155	2	3.864	EX
τ_0	0.5	0.433	0.25	0.1295	
T	0.6092	0.6094	0.6082	0.6078	0.6065
T_s	0.1474	0.1478	0.1488	0.1486	0.1486
T'	0.7753	0.7757	0.7753	0.7750	0.7749
τ_0	1	0.866	0.5	0.259	
T	0.3705	0.3724	0.3719	0.3716	0.3679
T_s	0.1777	0.1789	0.1781	0.1800	0.1803
T'	0.5981	0.5995	0.5990	0.6003	0.6005
τ_0	2	1.732	1	0.518	
T	0.1337	0.1344	0.1333	0.1352	0.1353
T_s	0.1322	0.1308	0.1343	0.1334	0.1326
T'	0.3523	0.3537	0.3552	0.3564	0.3606
τ_0	4	3.464	2	1.036	
T	0.0162	0.0175	0.0181	0.0189	0.0183
T_s	0.0338	0.0338	0.0343	0.0368	0.0359
T'	0.1195	0.1224	0.1242	0.1297	0.1300
τ_0	6	5.196	3	1.554	
T	0.0023	0.0020	0.0026	0.0018	0.0025
T_s	0.0075	0.0087	0.0063	0.0073	0.0073
T'	0.0431	0.0445	0.0459	0.0439	0.0469
τ_0	8	6.926	4	2.070	
T	0.00035	0.00015	0.0000	0.00032	0.00034
T_s	0.0010	0.0006	0.0013	0.0011	0.0013
T'	0.0184	0.0129	0.0143	0.0153	0.0168
τ_0	10	8.658	5	2.588	
T	0.0000	0.0000	0.00012	0.00015	0.00005
T_s	0.00022	0.00022	0.00012	0.00007	0.00022
T'	0.0061	0.0054	0.0049	0.0053	0.0060

$P\Delta\Omega = 0.489$
$\bar{\omega} = 0.99999$

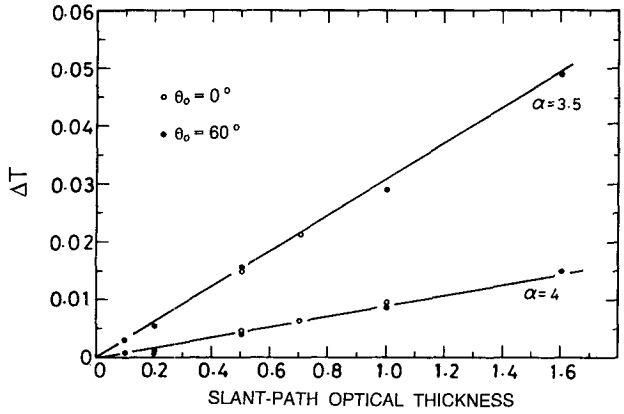

FIG. 7. Apparent transmission ratio, ΔT defined by Eq. (17), for aerosol scattering versus the slant-path optical thickness. The power-law size distributions with the power $\alpha = 3.5$ and 4.0 are assumed. Open and solid circles indicate the Monte Carlo simulations with $\theta_0 = 0°$ and 60°, respectively. Solid lines are drawn by Eq. (19).

sults for several FOVs. The amounts of $P\Delta\Omega$ for the TL phase function with the FOV of $\eta_0 = 0.5°$, 1.2°, and 2.0° are 0.376, 0.489, and 0.536, respectively. The simulations shown by symbols in the figure agree well with the lines that were drawn by Eqs. (14) and (21), and the parameterization is good for various FOVs.

b. *Observational results*

We observed cirrostratus clouds over Tsukuba on 22 and 30 June 1989. For the 22 June case, the cloud-bottom height detected by lidar and HYVIS was about 7 km and the temperature at that height was −20°C. The cloud reached the tropopause at the 13-km height. Existence of ice columns with the maximum dimension of 20 μm to 1 mm was observed by the HYVIS, which is capable of obtaining images of ice crystals between about 10 μm and 1 cm using two balloon-borne TV cameras (Mizuno et al. 1992). A 22° halo observed from the ground also supported their existence. The observational situation for the 30 June case was close to the former case because the cirrostratus clouds were generated by similar warm front activities on both days.

Heymsfield and Platt (1984) have found that the particle size distribution of ice clouds is expressed by a power-law function given by

$$n(L) = CL^{-\alpha}, \qquad (22)$$

where L is the maximum dimension and C is a constant. The size distribution of ice crystals measured by the HYVIS was approximated by a power-law size distribution after their expression. The least-squares fit to the HYVIS measurement has estimated the power to be $\alpha = 3.2$ (Uchiyama et al. 1993).

Radiation measurements were simultaneously acquired with the ground-based instruments. Figure 9a shows a time series of the optical thickness at $\lambda = 0.5$ μm for cirrostratus measured by the sun photometer. The cloud optical thickness was corrected by Eq. (20) with the value $k = 0.51$ based on simulations for a cirrostratus model presented by TL. The aerosol optical thickness at $\lambda = 0.5$ μm for the 22 and 30 June cases, which should be subtracted in the analyses, was estimated to be 0.5 and 0.3, respectively, from measurements under cirrus-free conditions on the same day. The variation of the broadband solar flux (Fig. 9b) measured by a pyranometer (Eko MS801) with a WG305 filter dome is well correlated conversely with the variation of the optical thickness.

c. *Relationship between the visible optical thickness and the broadband solar flux transmittance*

Figure 10 shows the diffuse flux transmittance and reflectance calculated for modeled ice clouds with the TL and HG phase functions as a function of the cloud optical thickness. The asymmetry factor $g = 0.75$ for the HG phase function is based on the original TL phase function. In spite of the large difference between the phase functions of TL and HG, as shown in Fig. 3, the results shown by the solid curves, which have the same value of the asymmetry factor, are very close to each other, within a 0.02 difference. Therefore, we

TABLE 3. Simulations for nonconservative scattering cases with $\bar{\omega} = 0.9$, 0.8, and 0.6. The Monte Carlo results for T, T_s, and T' in column MC are compared with those in column EX, which were calculated by Eq. (1), Eq. (16), and Eqs. (14) and (21), respectively.

$\bar{\omega}$	0.9		0.8		0.6	
	MC	EX	MC	EX	MC	EX
$\tau_0 = 0.5$						
T	0.6094	0.6065	0.6094	0.6065	0.6094	0.6065
T_s	0.1322	0.1337	0.1175	0.1189	0.0882	0.0892
T'	0.7570	0.7562	0.7390	0.7379	0.7043	0.7026
$\tau_0 = 1$						
T	0.3708	0.3679	0.3708	0.3679	0.3711	0.3679
T_s	0.1600	0.1623	0.1422	0.1442	0.1065	0.1082
T'	0.5716	0.5718	0.5446	0.5444	0.4947	0.4936
$\tau_0 = 2$						
T	0.1346	0.1353	0.1345	0.1353	0.1334	0.1353
T_s	0.1191	0.1193	0.1058	0.1061	0.0796	0.0796
T'	0.3235	0.3269	0.2936	0.2964	0.2411	0.2437
$\tau_0 = 4$						
T	0.0177	0.0183	0.0175	0.0183	0.0168	0.0183
T_s	0.0295	0.0323	0.0262	0.0287	0.0193	0.0215
T'	0.1001	0.1069	0.0824	0.0879	0.0554	0.0594
$\tau_0 = 6$						
T	0.0023	0.0025	0.0020	0.0025	0.0032	0.0025
T_s	0.0065	0.0066	0.0053	0.0058	0.0044	0.0044
T'	0.0348	0.0349	0.0250	0.0260	0.0153	0.0145

$P\Delta\Omega = 0.489$
$\theta_0 = 0°$

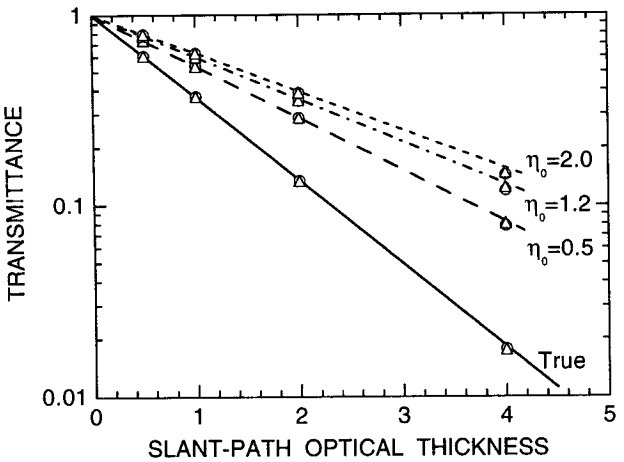

FIG. 8. Apparent transmittances simulated with the half-FOV η_0 = 0°, 0.5°, 1.2°, and 2.0° for several slant-path optical thicknesses. Circles and triangles indicate the Monte Carlo results for θ_0 = 0° and 60°, respectively. The broken, dot–broken, and short-dashed lines are drawn by Eqs. (14) and (21), corresponding to the simulations indicated by symbols for η_0 = 0.5°, 1.2°, and 2.0°, respectively. The solid line indicates the true transmittance (or η_0 = 0°) given by Eq. (1).

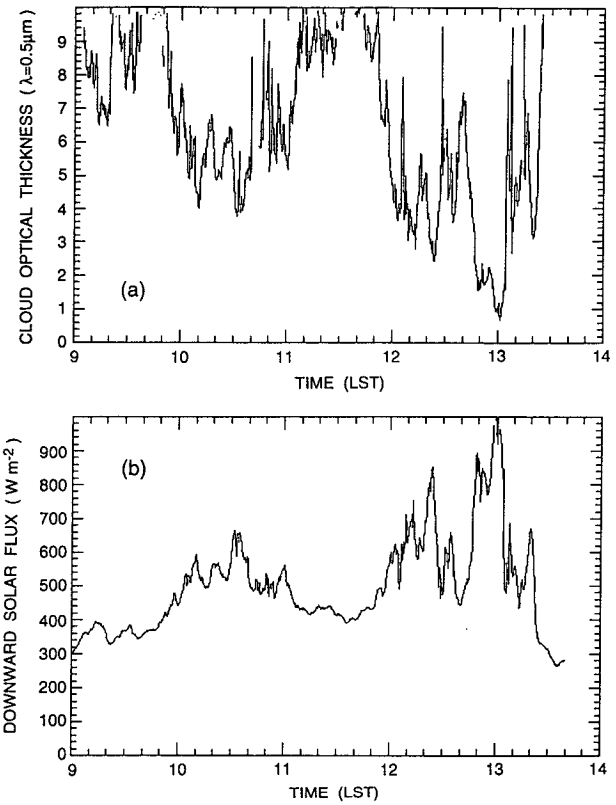

FIG. 9. Observational results for cirrostratus on 22 June 1989. (a) Cloud optical thickness at λ = 0.5 μm, and (b) downward flux of solar radiation.

can use the HG phase function in place of the exact phase function for the radiative flux calculation if we choose g equal to the value from the exact phase function. On the other hand, the comparison between the results for g = 0.75 (solid curves) and 0.85 (broken curves) certifies that the radiative flux strongly depends on the asymmetry factor of the phase function.

Figure 11 shows the relationship between the optical thickness at λ = 0.5 μm and the broadband solar flux transmittance. The transmittance was derived from the measured downward solar radiative flux F_s (W m^{-2}), shown in Fig. 9 through the following relation:

$$T = \frac{F_s R^2}{F_0 \cos\theta_0}, \qquad (23)$$

where R is the sun–earth distance in astronomical units, and F_0 is the direct solar irradiance at the top of the atmosphere, 1318 W m^{-2} for the spectral range of 0.3–2.8 μm where the pyranometer is sensible. Observational data indicated by dots are restricted to those obtained during 1100–1200 LST in order to eliminate effects due to variation of the solar zenith angle. Simulated results for the HG phase functions with two different asymmetry factors are compared with the observational results in the same figure. The calculations were made by the doubling–adding method described in some detail in Asano and Shiobara (1989) under the following conditions. The solar zenith angle was 13°, the value at the local noon of the day. A Lambertian surface was assumed to have the surface albedo A = 0.08 for λ < 0.7 μm and 0.13 for λ > 0.7 μm. Radiosonde data at 0900 LST from the Tateno Aerological Observatory, about 200 m north of the MRI, were utilized for the atmospheric profile in the calculation. The calculations include the aerosol scattering for which the optical thickness is assumed to be 0.3 at λ = 0.5 μm and a power-law size distribution with α = 4 is assumed. In the figure, the curve with circles

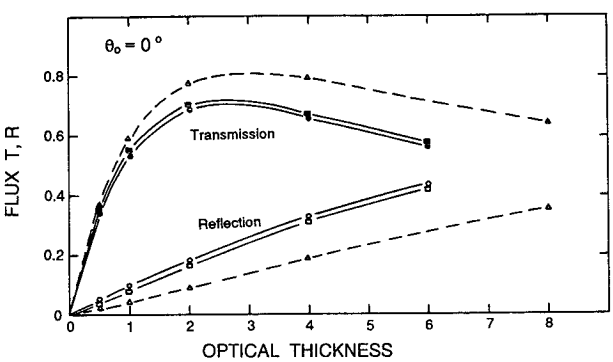

FIG. 10. The diffuse flux transmittance and reflectance versus the cloud optical thickness. Solid curves with solid and open circles indicate the diffuse transmittance and reflectance, respectively, using the TL phase function. Solid curves with rectangles indicate those using the HG phase function with g = 0.75. Broken curves indicate those using the HG function with g = 0.85.

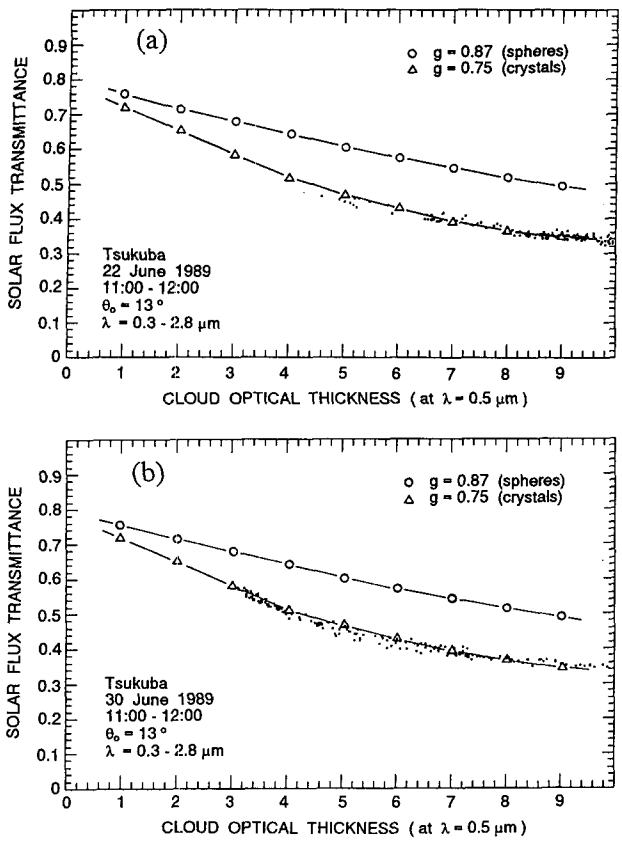

FIG. 11. Relationship between the cloud optical thickness at $\lambda = 0.5$ μm and the broadband solar flux transmittance. The measurements plotted by dots are restricted during 1100–1200 LST. Crosses indicate calculations with the HG phase function with $g = 0.75$, while circles indicate calculations with $g = 0.85$; (a) for the 22 June case, and (b) for the 30 June case.

indicates the calculated transmittance obtained by using the HG phase function with the asymmetry factor $g = 0.87$ at $\lambda = 0.5$ μm. The value of g was calculated from Mie theory for ice spheres with the radius $r = 4$–200 μm where the power α in Eq. (22) was zero for $r = 4$–5 μm, and 3.5 for $r = 5$–200 μm. The other curve with triangles indicates the result calculated with the adjusted asymmetry factors, that is, the asymmetry factor at $\lambda = 0.5$ μm was 0.75 from the TL phase function, and its wavelength dependence in the spectral range of 0.3–2.8 μm was assumed to follow that of the asymmetry factors computed for the ice sphere model. The transmittance calculated theoretically by assuming ice spheres are larger than the observed values by more than 10%. On the other hand, the transmittance calculated with the modified asymmetry factors agreed well with the observed values within 4% in the region of the optical thickness of 3–10. The result implies that ice spheres should not be assumed for calculations of radiative transfer in ice clouds. When ice spheres are assumed, very small particles of submicron-order should be contained in the ice cloud in order to have such a small value of $g = 0.75$. It is also suggested that the asymmetry factors of the cirrostratus clouds during the June 1989 experiment in Tsukuba were almost the same as that of the TL phase function.

d. Discussion of errors

Here, we discuss the source and amount of errors involved in the cirrus optical thickness measured by the sun photometer. The error due to instrumental calibration is relatively small in cloud observations since an error of 2% in the calibration constant causes only 0.02 or less change to the optical thickness. In the same manner, errors due to fitting with Eq. (14) to the apparent transmittance do not cause significant errors in the optical thickness. The surface albedo was assumed to be zero in the present simulation. Several results with the assumption of $A = 0.15$ have caused no significant difference in the apparent optical thickness as shown in Table 4. The effect of finiteness of the solar disk was roughly investigated by calculations with small changes of the solar zenith angle. The error due to the finiteness was not distinguishable from the Monte Carlo error. The ambiguity in the FOV may cause an appreciable error relating to a change of the forward scattering phase function around the FOV. For the present case, the difference of $P\Delta\Omega$ between $\eta_0 = 1.0$ and 1.5 is 0.03, so that an erroneous FOV may not cause significant errors in the optical thickness. It should be noticed, however, that the error depends on the shape of the phase function in the forward direction and that the correction method proposed in this study essentially needs an exact profile of the cloud phase function. In other words, the correction coefficient for sun photometry derived here depends on the phase function. Only the TL phase function is used for ice clouds in this study. There is no confidence that the TL phase func-

TABLE 4. Comparisons between the results for the cases with surface albedos $A = 0$ and 0.15; T, T_s, and T' in column EX are calculated by Eq. (1), Eq. (16), and Eqs. (14) and (21), respectively.

		$\theta_0 = 0°$		$\theta_0 = 60°$		
	A	0	0.15	0	0.15	EX
$\bar{\tau}_0 = 0.5$	T	0.6092	0.6060	0.6082	0.6106	0.6065
	T_s	0.1474	0.1504	0.1488	0.1426	0.1486
	T'	0.7753	0.7759	0.7753	0.7719	0.7749
$\bar{\tau}_0 = 2$	T	0.1337	0.1347	0.1333	0.1339	0.1353
	T_s	0.1322	0.1278	0.1343	0.1348	0.1326
	T'	0.3523	0.3574	0.3552	0.3583	0.3606
$\bar{\tau}_0 = 4$	T	0.0162	0.0146	0.0181	0.0167	0.0183
	T_s	0.0338	0.0368	0.0343	0.0382	0.0359
	T'	0.1195	0.1200	0.1242	0.1246	0.1300

$P\Delta\Omega = 0.489$
$\bar{\omega} = 0.99999$

tion is representative for ice clouds in general. The amount of error due to the difference of the cloud microphysics is thus not estimated in this study, because dependence of the phase function on microphysical properties of ice clouds is not clearly known at present.

5. Summary

An extensive radiative transfer calculation was carried out to simulate sun photometer observations of cirrus clouds. The Monte Carlo method (Figs. 1 and 2) was applied in the simulations, in which the scattering phase function for ice crystals calculated by Takano and Liou (1989) was employed.

As shown in Fig. 6 and Table 2, the apparent solar transmittance is much larger than the true value because the sun photometer receives not only the attenuated direct irradiance but also radiance scattered into the instrument's FOV. On the other hand, we found that the forward scattering effect is negligibly small for ordinary aerosols (Fig. 7) because the aerosol scattering phase function has a forward peak much smaller than that for ice crystals (Fig. 3).

A simple relationship between the true and apparent optical thicknesses, as expressed by Eq. (20), was derived for cases of both ice clouds and aerosols. The result shows that the apparent transmittance including radiance scattered into the FOV can be parameterized with the slant-path optical thickness when the scattering phase function of ice clouds is known. The correction method was successfully applied to sun photometer measurements for cirrostratus clouds observed over Tsukuba.

The exact phase function may be replaced by a Henyey–Greenstein phase function in calculations of radiative flux if the HG phase function has the exact asymmetry factor (Fig. 10).

A relationship between the broadband solar flux transmittance and the visible optical thickness was obtained for cirrostratus clouds observed on 22 and 30 June 1989 in Tsukuba. The measurement was compared with the theoretical calculation. The result shown by Fig. 11 implies that ice spheres should not be assumed for calculations of radiative transfer in ice clouds. Further, the measurement agreed well with simulations using the phase function by Takano and Liou (1989), indicating that the asymmetry factors for the cirrostratus clouds observed during the June 1989 experiment happened to be almost the same as that of the Takano–Liou phase function for a cirrostratus model.

The shape and size distribution of ice crystals are responsible for the scattering phase function. Therefore, precise information on the cloud microphysics is essential to improve accuracy of the optical thickness estimation from sun photometry.

Acknowledgments. The authors express their sincere thanks to Dr. James D. Spinhirne for encouraging this study and kindly reviewing this paper. Discussions with Drs. Teruyuki Nakajima, Stefan Kinne, and Akihiro Uchiyama, and their helpful comments are also acknowledged.

REFERENCES

Asano, S., and M. Shiobara, 1989: Aircraft measurements of the radiative effects of tropospheric aerosols: I. Observational results of the radiation budget. *J. Meteor. Soc. Japan,* **67,** 847–861.

FIRE, 1990: Fire science results 1989. NASA Conf. Publication 3079, 506 pp.

Heymsfield, A. J., 1975: Cirrus uncinus generating cells and the evolution of cirriform clouds. *J. Atmos. Sci.,* **32,** 799–808.

——, and C. M. R. Platt, 1984: A parameterization of the particle size spectrum of ice clouds in terms of the ambient temperature and the ice water content. *J. Atmos. Sci.,* **41,** 846–855.

ICE, 1989: *ICE—International Cirrus Experiment 1989 Field Phase Plan.* Inst. Geophys. Meteorol., Univ. Köln, 97 pp.

Mizuno, H., T. Matsuo, M. Murakami, and Y. Yamada, 1992: Microstructure of cirrus clouds observed by HYVIS. *Proc. 11th Int. Conf. on Clouds and Precipitation,* Montreal, Amer. Meteor. Soc., 488–491.

Murakami, M., and T. Matsuo, 1990: Development of the hydrometeor videosonde. *J. Atmos. Oceanic Technol.,* **7,** 613–620.

Raschke, R. A., and S. K. Cox, 1983: Instrumentation and technique for deducing cloud optical depth. *J. Climate Appl. Meteor.,* **22,** 1887–1893.

Takano, Y., and K.-N. Liou, 1989: Solar radiative transfer in cirrus clouds. Part I: Single-scattering and optical properties of hexagonal ice crystals. *J. Atmos. Sci.,* **46,** 3–19.

Uchino, O., I. Tabata, K. Kai, and Y. Okada, 1988: Polarization properties of middle and high level clouds observed by lidar. *J. Meteor. Soc. Japan,* **66,** 607–616.

Uchiyama, A., S. Asano, M. Shiobara, and M. Fukabori, 1993: Ground-based observation of cirrostratus clouds: Spectral properties of cirrus clouds in the 8–12 μm. *Clouds and Ocean in Climate—Extented Abstracts of Int. WCRP Symp.,* Nagoya. Nagoya University, 8.24–8.27. [Available from Institute for Hydrospheric–Atmospheric Sciences, Nagoya University, Furo-Cho, Chikusa, Nagoya 464-01, Japan.]

van de Hulst, H. C., 1980: *Multiple Light Scattering. Tables, Formulas, and Applications.* Vol. 2. Academic Press, 739 pp.

WENPEX/MRI, 1992: A synthetic study on cloud-radiation processes. MRI Tech. Rep., No 29. Meteorological Research Institute, Tsukuba, Japan, 340 pp (in Japanese with English summary and figure captions). [Available from Meteorological Research Institute, 1-1 Nagamine, Tsukuba 305, Japan.]